Materials Characterization 235 (2026) 116267

Contents lists available at ScienceDirect

Materials Characterization

journal homepage: www.elsevier.com/locate/matchar

Dissimilar fusion welding of NiTi shape memory alloy and $AlCoCrFeNi_{2.1}$ eutectic high entropy alloy using multi-interlayer strategy

Nithin Joseph Reddy Sagili Arthur [a,*], Rae Eon Kim [b], Ana Martins [a], Hyoung Seop Kim [b,d], N. Schell [c], João Pedro Oliveira [a,*]

[a] CENIMAT/I3N, Department of Materials Science, NOVA School of Science and Technology, Universidade NOVA de Lisboa, Caparica 2829-516, Portugal
[b] Graduate Institute of Ferrous and Eco Materials Technology, POSTECH (Pohang University of Science and Technology), Pohang 37673, South Korea
[c] Institute of Materials Physics, Helmholtz-Zentrum Hereon, Max-Planck-Str. 1, 21502 Geesthacht, Germany
[d] Advanced Institute for Materials Research (WPI-AIMR), Tohoku University, Sendai 980-8577, Japan

ARTICLE INFO

Keywords:
Dissimilar fusion welding
NiTi shape memory alloy
$AlCoCrFeNi_{2.1}$ eutectic high entropy alloy
Multi-interlayer diffusion barrier
Thermodynamic simulation
Synchrotron X-ray diffraction
Mechanical characterization

ABSTRACT

Dissimilar fusion welding between NiTi shape memory alloy and $AlCoCrFeNi_{2.1}$, eutectic high entropy alloy was achieved using a combination of Nb and Cu interlayers. Both base metals exhibit unique properties that complement each other making them attractive for integration in smart systems. However, direct joining of these materials is not feasible due to the formation of brittle intermetallic compounds that compromise the joint integrity. Thus, to avoid this metallurgical issue dissolution of the Nb and Cu interlayers promoted elemental intermixing and altered solidification pathways, leading to the formation and intensification of topologically close-packed phases. Phase evolution was assessed through thermodynamic CALPHAD simulations and validated using synchrotron X-ray diffraction, while further microstructural characterization employed backscattered electron imaging and energy dispersive spectroscopy. The weld exhibited pronounced spatial heterogeneity, with a peak hardness of 856 $HV_{0.3}$ near the NiTi-side interfacial region, consistent with enrichment of TCP phases and Ti-rich intermetallics. Tensile testing showed fracture at an ultimate tensile strength of 372 MPa and a fracture strain of 1.11%, with crack initiation in the hardened interfacial region followed by mixed-mode fracture toward the fusion zone. Although tensile ductility remains limited, the multi-interlayer strategy enabled defect-free joint formation and confined embrittlement to a narrow region compared with direct joining.

1. Introduction

Advanced materials such as shape memory alloys (SMA) and high entropy alloys (HEA) offer functionalities that surpass the capabilities of conventional alloys. In particular, NiTi SMA and $AlCoCrFeNi_{2.1}$, eutectic high entropy alloy (EHEA) have attracted considerable attention due to their potential in demanding engineering applications. Combining these alloys in a dissimilar configuration is especially promising for smart systems, as it enables the integration of distinct functionalities, leading to design flexibility and potential cost savings [1–4]. However, joining these materials pose substantial challenges due to their chemical, crystallographic and thermophysical disparities [5,6]. As a result, the use of interlayers or filler materials is often necessary to obtain a viable weld joint. In this study, we explore the dissimilar joining of NiTi SMA and $AlCoCrFeNi_{2.1}$ EHEA using a multi-interlayer strategy designed to mitigate these challenges.

A brief overview of the base alloys and their weldability provides the necessary context. NiTi, a widely used SMA with near-equiatomic composition, finds applications in automotive, biomedical, and aerospace sectors due to its ability to function as both structural and active material [7–9]. It exists in either the high-temperature austenitic B2 phase or the low-temperature martensitic B19′ phase. Deviations from stoichiometry, however, promote the formation of detrimental intermetallics such as Ti_2Ni and Ni_3Ti, which degrade the material functional properties [10]. Welding of NiTi remains challenging, as exposure to high temperatures, elemental evaporation, and non-equilibrium solidification often induce complex microstructures and unexpected phase transformations along the weld [11–16]. To overcome these issues, interlayers have been widely employed, acting either as diffusion barriers or as dilution modifiers to control weld pool chemistry [17–34]. A comprehensive list of NiTi dissimilar welds with corresponding tensile strength and intermetallic formation, is provided in Appendix A,

* Corresponding authors.
E-mail addresses: n.arthur@campus.fct.unl.pt (N.J.R.S. Arthur), jp.oliveira@fct.unl.pt (J.P. Oliveira).

https://doi.org/10.1016/j.matchar.2026.116267
Received 10 November 2025; Received in revised form 22 December 2025; Accepted 11 March 2026
Available online 12 March 2026

Table A.1.

High entropy alloys are a novel class of alloys containing multiple principal elements, typically in the range of 5–35 at.% [35,36]. Their high configurational entropy favours solid solution formation over intermetallic compounds. To overcome the strength–ductility trade-off in single-phase high entropy alloys (HEA), dual-phase EHEA were developed. Among them, $AlCoCrFeNi_{2.1}$ stands out due to its excellent strength, corrosion resistance, and large-scale castability [37,38]. Like NiTi, it exhibits dual functionality, serving as both structural and functional material, making it highly versatile [39,40]. Although the fusion weldability of $AlCoCrFeNi_{2.1}$ is still under exploration, existing studies indicate improved tensile and corrosion properties in the welded joints compared to the base alloy [41–44]. To the author's best knowledge only three studies have been conducted on dissimilar welding of $AlCoCrFeNi_{2.1}$ alloys (with austenitic stainless steels) [45–47], demonstrating good weldability even without the use of filler materials. This highlights the potential of $AlCoCrFeNi_{2.1}$ for integration with other alloys in novel dissimilar configurations.

Gas tungsten arc welding (GTAW) is a relatively simple and cost-effective arc based fusion welding process that has led to large scale industrialisation. Albeit much research on advanced materials focusses on high energy density welding process like laser and electron beam welding, GTAW offers several advantages. The reduced capital investment, lower operational cost, open operating environment and ability to automate makes this process promising for fabricating advanced class of materials. The functional similarities between NiTi and $AlCoCrFeNi_{2.1}$ make them a unique combination for real world applications, where each can reinforce and complement the other. Potential applications include vibration damping in automotive shock absorbers and seismic mitigation in civil engineering.

Despite extensive research on NiTi dissimilar welding and the growing interest in eutectic high-entropy alloys, no prior study has reported the dissimilar fusion welding of NiTi shape memory alloy with $AlCoCrFeNi_{2.1}$ eutectic high-entropy alloy. In this work, a Nb—Cu multi-interlayer strategy coupled with arc-offset GTAW is employed to enable defect-free dissimilar joining of these alloys. The scientific contribution of this study lies in establishing a comprehensive process–structure–property relationship by integrating CALPHAD-based solidification simulation, high-energy synchrotron X-ray diffraction, detailed microstructural characterization, and mechanical testing. The results provide new insights into the role of interlayer-mediated dilution in controlling phase formation, strain partitioning, and embrittlement localization in highly dissimilar advanced alloy weld systems.

2. Materials and methodology

2.1. Materials

NiTi cold rolled sheets of 1.5 mm thickness in the austenite phase, manufactured according to ASTM F2063–18 specification were procured commercially. $AlCoCrFeNi_{2.1}$ eutectic high entropy alloy was prepared by melting Al, Co and Ni elements with 99.9 wt% purity, along with Cr and Fe with 99.5 wt% purity. The as-cast alloy was remelted multiple times to ensure chemical homogeneity. The resulting cast block was sectioned into 1.5 mm thick sheets using wire electrical discharge machining (WEDM). Both materials were then cut to 40 × 40 × 1.5 mm weld coupons using a slow speed precision cutting machine. A refractory interlayer of niobium (Nb) with 0.05 mm thickness and a copper (Cu) interlayer of 0.1 mm thickness were positioned at the abutting edges in a square groove butt joint fit-up as shown in Fig. 1. The commercially procured interlayers had 99.9 wt% purity. All materials were manually polished using SiC abrasive papers to remove oxide layers and were further cleansed ultrasonically in an acetone bath. Table 1, provides the chemical composition of the base metals. The measured composition of the NiTi base metal agrees well with the nominal values, while a deviation was observed in the $AlCoCrFeNi_{2.1}$ base metal due to preferential loss of Al due to its relatively low melting point.

2.2. Welding process

Gas tungsten arc welding was performed using an in-house built cartesian kinematic machine. The weld schematic and joint fit-up are shown in Fig. 1. A straight polarity (or) direct current electrode negative (DCEN) configuration with a heat input of 169.02 J/mm (with at least 75% efficiency) was used to coalesce the abutting edges, the corresponding welding parameters are summarized in Table 2, optimized through multiple bead on plate trials. Argon inert shielding gas of 99.9% purity characterized by high ionization potential and low thermal conductivity was used to effectively shield the weld pool from atmospheric contamination. The shielding was provided at the face, root as well as along the trailing edge of weld pool. Due to the disparate material properties, arc offset welding (AOW) was employed by displacing the weld torch 1.0 mm toward the eutectic high entropy alloy, which has a higher melting temperature of approximately 40 °C than NiTi (1350 °C vs 1310 °C). This offset technique was used to control the elemental migration and solubility. Additionally the excess multi-interlayer at the abutting edges were covered on to the NiTi shape memory alloy to provide effective shielding from the weld arc.

2.3. Microstructural characterization

Samples for microstructural analysis were obtained by sectioning the weld joint traverse to the weld direction. The cut sample were then cold mounted using epoxy resin and polished with SiC abrasive in colloidal alumina and silica solutions. Polished samples were cleansed with acetone to remove any residues and dried thoroughly. An etchant of HF: HNO_3:H_2O in a 10:25:150 volume ratio was used to reveal the microstructure. A Leica DMI 5000 M inverted optical microscope (OM) was used to obtain the microstructure. A JEOL JEM 2100F fast emission scanning electron microscope (SEM) with a JEOL 54230RBED, back scatter electron (BSE) detector was used for high resolution BSE imaging and energy dispersive spectroscopy (EDS) using a X-Max EDS detector

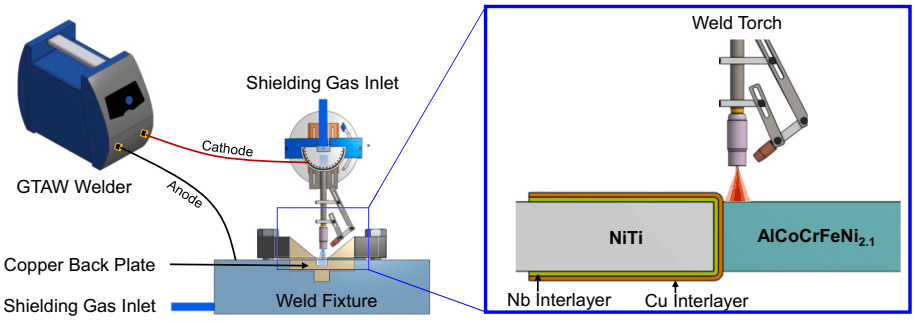

Fig. 1. Weld setup schematic and joint fit-up (enlarged view).

Table 1
Base metal chemical composition.

Material		Elements (at. %)					
		Al	Co	Cr	Fe	Ni	Ti
NiTi	Nominal	–	–	–	–	50.8	49.2
	Measured	–	–	–	–	50.9	49.1
AlCoCrFeNi2.1	Nominal	16.39	16.39	16.39	16.39	34.44	–
	Measured	14.69	16.91	16.63	16.68	35.09	–

Table 2
GTAW Welding parameters.

Current (ampere)	Voltage (volt)	Travel speed (mm/s)	Shielding gas flow rate (l/min)		Heat input (J/mm)
			Face (Incl. Trailing edge)	Root	
63	12.5	3.5	15	10	169.02

along with Aztec energy software for chemical composition analysis.

2.4. Thermodynamic-CALPHAD simulation

CALPHAD-based thermodynamic simulations were performed using Thermocalc Software with the TCHEA 5.1 database [48]. The classic Scheil-Gulliver model was employed to simulate the non-equilibrium solidification nature of the weld. These results were then correlated with synchrotron X-ray diffraction data to confirm the phase evolution and transformations across the weld joint.

2.5. Synchrotron X-ray diffraction

High energy synchrotron X-ray diffraction (SXRD) was conducted at P07 High Energy Materials Science beamline at PETRA III, DESY. A monochromatic radiation of 87 keV corresponding to a wavelength of 0.14235 Å, was directed at the sample through a 0.2 × 0.2 mm slit. Scans were performed at 0.2 mm intervals linearly across the weld joint, starting from one of the base materials and transversing the joint until reaching the opposite side, as shown in Fig. 2. The resulting 2D diffraction patterns were recorded on a PerkinElmer fast detector. The Debye-Scherrer rings were then processed using Fit2D [49], MDI Jade [50] and PDF-5+ software's [51]. Williamson–Hall (W—H) analysis was further applied to the SXRD data to quantify the microstrain and crystallite size across the fusion zone.

2.6. Mechanical characterization

A Shimadzu tensile tester equipped with 50kN load cell was used to perform tensile testing at a strain rate of 1×10^{-3} s^{-1}. The fractured surfaces were then assessed using a Hitachi TM3030 Plus tabletop field emission scanning electron microscope. Vickers microhardness testing was performed using a Zwick Roell Indentec hardness testing machine with a 300-gf load and 10 s dwell time. Indentations were made across the weld zone at a longitudinal and traverse spacing of 0.2 × 0.2 mm.

3. Results and discussion

3.1. Microstructural evolution and solidification

The interlayers were placed in a tailored configuration at the abutting edges as illustrated in the schematic of Fig. 1, with their selection and positioning guided by their metallurgical compatibility. The NiTi-Nb system exhibits a eutectic reaction at 1170 °C, and both Nb and Cu can substitute for Ni in the NiTi lattice [9,52]. Moreover, Nb and Cu are known to form ternary shape memory alloys with NiTi, reinforcing their suitability as interlayers. Conversely, Nb tends to form C14 Laves phase with $AlCoCrFeNi_{2.1}$ and can promote σ phase formation, whereas Cu shows only limited solubility in the AlCoCrFeNi system [53,54]. Importantly, the Cu—Nb binary system undergoes a peritectic reaction at 1093 °C but does not form intermetallic compounds [55]. Based on these considerations, Nb was placed adjacent to NiTi to act as a diffusion barrier, while Cu was placed adjacent to $AlCoCrFeNi_{2.1}$, to suppress intermetallic formation and ensure joint integrity.

A defect free weld joint was achieved, as confirmed by the microstructural analysis shown in Fig. 3. At the centre of the weld, a slight reduction in cross sectional area is visible, attributed to the high velocity ionic plasma jet displacing liquid metal radially outward [56,57]. The

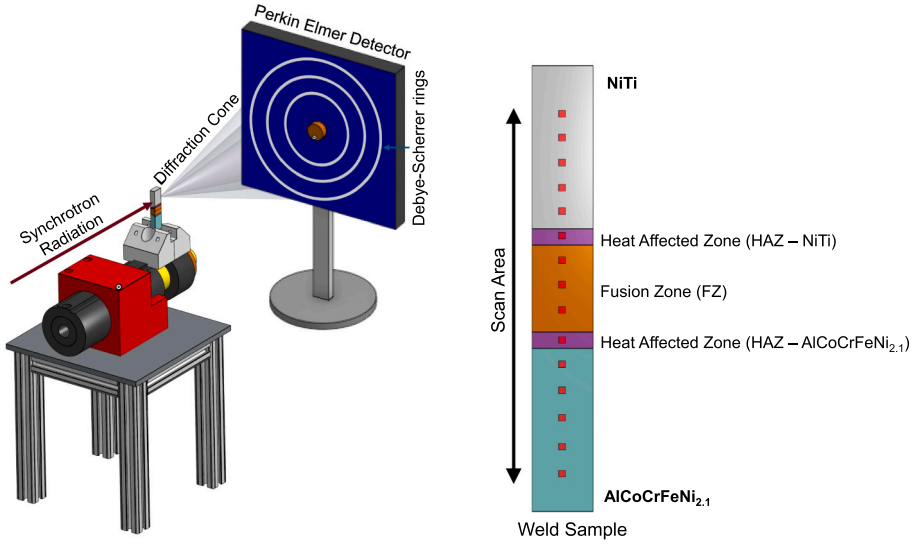

Fig. 2. Synchrotron X-ray diffraction experimental setup and scanning schematic.

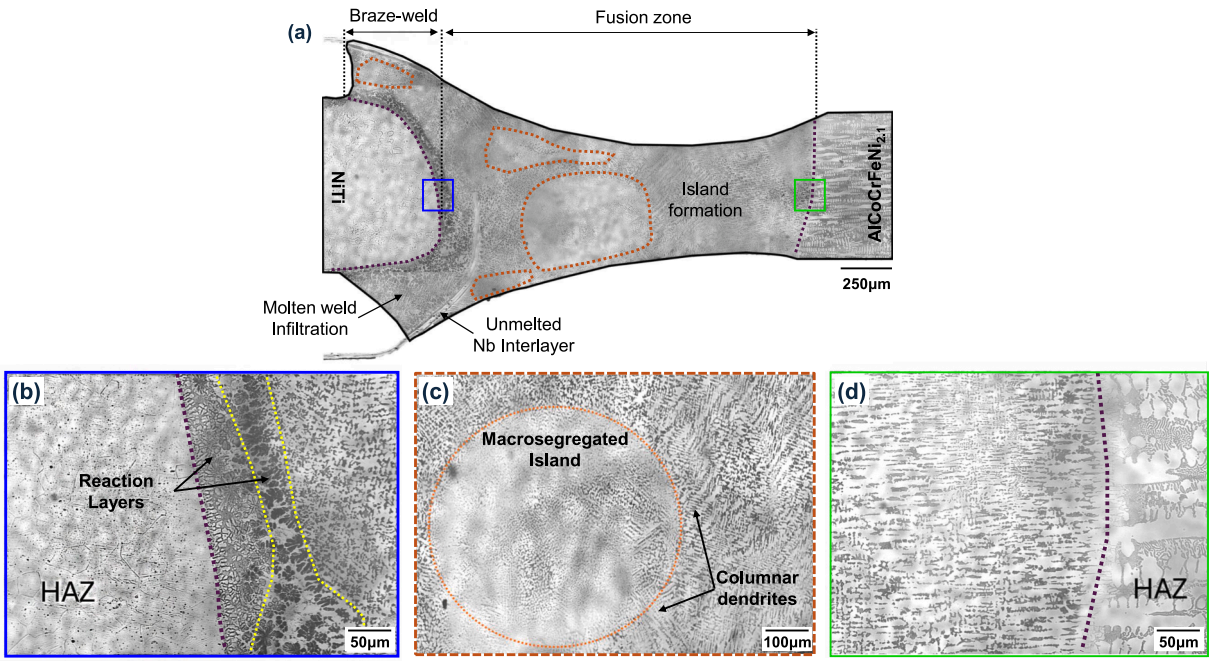

Fig. 3. Weld joint microstructure. a) Microstructure map; b)NiTi HAZ and fusion zone interface; c) Macrosegregation (close-up of island and surrounding region marked in (a)); d) Fusion zone and AlCoCrFeNi2.1 HAZ interface.

steep temperature gradient along the isothermal boundary, on reaching the melting point of both the interlayers, resulted in either partial or complete dissolution. Consequently, the Nb interlayer fails to act as a diffusion barrier, allowing elemental intermixing. Capillary forces further drove liquid infiltration between the NiTi base metal and the interlayer. Hence, it is evident that the region beneath the weld arc undergoes fusion welding, whereas the abutting edges experienced a weld-brazing (WB) mechanism.

To interpret the evolution of reaction layers and macrosegregated islands observed in Fig. 3, the fluid flow and thermal gradient environment of the weld pool must be considered. The fluid flow in the bulk weld pool is governed by Marangoni convection, which arises from surface tension gradients influenced by both temperature and composition. As illustrated in Fig. 4, the NiTi interface experiences more turbulent or toroidal convection compared to $AlCoCrFeNi_{2.1}$ interface, owing to compositional asymmetry. Similar convection-driven behaviour has been reported in dissimilar welds of Cu with Ni and maraging steel [58,59]. This convective circulation strongly influences elemental diffusion, which can be described by Fick's second law for spatio-temporal concentration gradients.

$$\frac{\partial C(x,t)}{\partial t} = \nabla\cdot[D(T(x,t))\nabla C(x,t)]$$

Where $\frac{\partial C}{\partial t}$ is the temporal rate of change of concentration and the $\nabla\cdot[D(T)\nabla C]$ is the divergence of diffusive flux. On the NiTi side, a steep thermal gradient (∇T) develops because NiTi, with its relatively high thermal conductivity of 18–28 W/m.k [60], compared to ~10 W/m.k of the EHEA (predicted by Thermocalc), acts as heat sink, rapidly extracting thermal energy from the fusion zone. This effect is further intensified by constitutional undercooling due to elemental intermixing. The limited heat retention time (t), restricts elemental diffusion (D(T)), producing sharp concentration gradients that manifest as reaction layers and macrosegregated islands. The reaction layer closest to the base metal undergoes only brief thermal exposure, insufficient for elemental partitioning, whereas layers closer to the weld centre remain at elevated temperatures longer, enabling segregation and multiphase formation. A similar suppression of diffusion under steep thermal gradients has been reported in other dissimilar weld systems [61]. Notably, no peninsula like protrusions were observed at the $AlCoCrFeNi_{2.1}$ fusion boundary. This absence is attributed to the extended diffusion of Cu in the fusion zone, a low melting point element that substantially increases the freezing range. The resulting wider solidification interval prolonged the presence of liquid phase allowing extended elemental intermixing and redistribution. This homogenized the weld pool chemistry and supressed compositional instabilities, thereby preventing peninsula formation. These effects are further supported by thermodynamic predictions presented in the subsequent sections.

Two distinct reaction layers at the NiTi interface as observed in Fig. 3

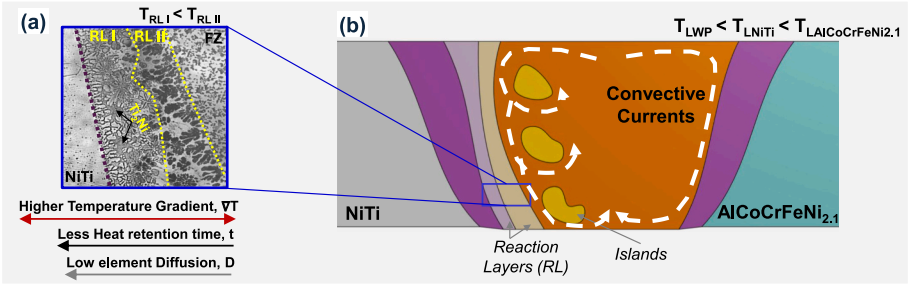

Fig. 4. Schematic of macrosegregation and interfacial reaction layers evolution in the fusion zone. a) effect of ∇T, t and D on reaction layers evolution and b) island formation.

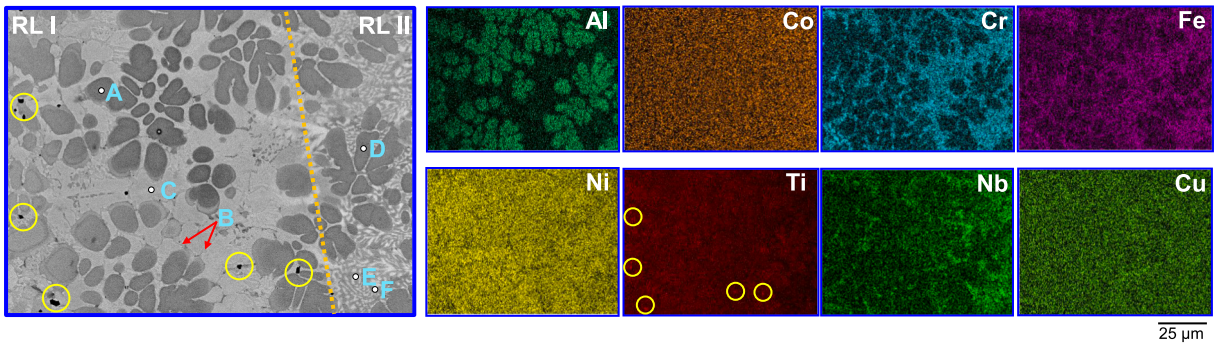

Fig. 5. BSE image of reaction layers with elemental mapping.

(b) and Fig. 4 (a), a phenomenon commonly observed in brazing [62]. The steep thermal gradient in this region restricts elemental diffusion, leading to transient intermetallic formation and compositional stratification. These layers were characterized using high resolution BSE imaging with elemental maps as shown in Fig. 5, and quantified through EDS analysis, shown in Table 3. Across both reaction layers Al, Ni and Ti (locations A and D) preferentially segregate within the dendritic regions, forming petal-like morphologies, stabilizing the B2 ($AlCoCrFeNi_{2.1}$) phase. Similar morphological transformations have been reported following Ti dissolution in $AlCoCrFeNi_{2.1}$ alloy [63]. Nb shows a strong tendency to enrich in the interdendritic regions together with Co, Cr and Fe (locations B and E) consistent with the formation of C14 Laves phase. This is in agreement with prior studies showing that transition metals such Nb and Zr promote C14 Laves phase in the $AlCoCrFeNi_{2.1}$ alloy [53,64]. Cu (locations C and F) also segregates at the interdendrites, coexisting with Co, Cr, Fe and Ni in a labyrinthic eutectic structure. Additionally, Ti-rich bands commonly observed in NiTi welding, as shown in Fig. 4, and as discrete precipitates marked in yellow circles shown in Fig. 5, confirm the presence of Ti-rich intermetallics.

Beyond the reaction layers, attention shifts to the bulk fusion zone where macrosegregated islands are present, as shown in Fig. 3 (c). Unlike the reaction layers, these regions show no petal-like morphologies and Nb enriched TCP phases, which is attributed to the restricted diffusion of Nb and Ti. Instead, a fine dendritic-interdendritic network is formed, with relatively higher Cu concentration compared to the reaction layers. EDS mapping and line scan (shown in Fig. 6) reveal that the

Table 3
Average elemental composition of reaction layers.

Location	Point	Elements, at. %							
		Al	Co	Cr	Fe	Ni	Ti	Nb	Cu
	A	11.9	7.7	2.7	4.3	42.7	25.8	1.0	3.9
RL I	B	1.7	10.0	17.3	14.7	28.0	20.9	4.9	2.5
	C	1.9	7.7	5.6	7.4	49.1	20.6	1.0	6.7
	D	17.4	10.5	3.7	5.1	38.4	17.8	3.0	4.2
RL II	E	1.8	13.1	17.3	15.4	25.7	14.2	10.7	1.8
	F	4.2	9.0	11.4	11.2	39.2	13.0	1.8	10.3

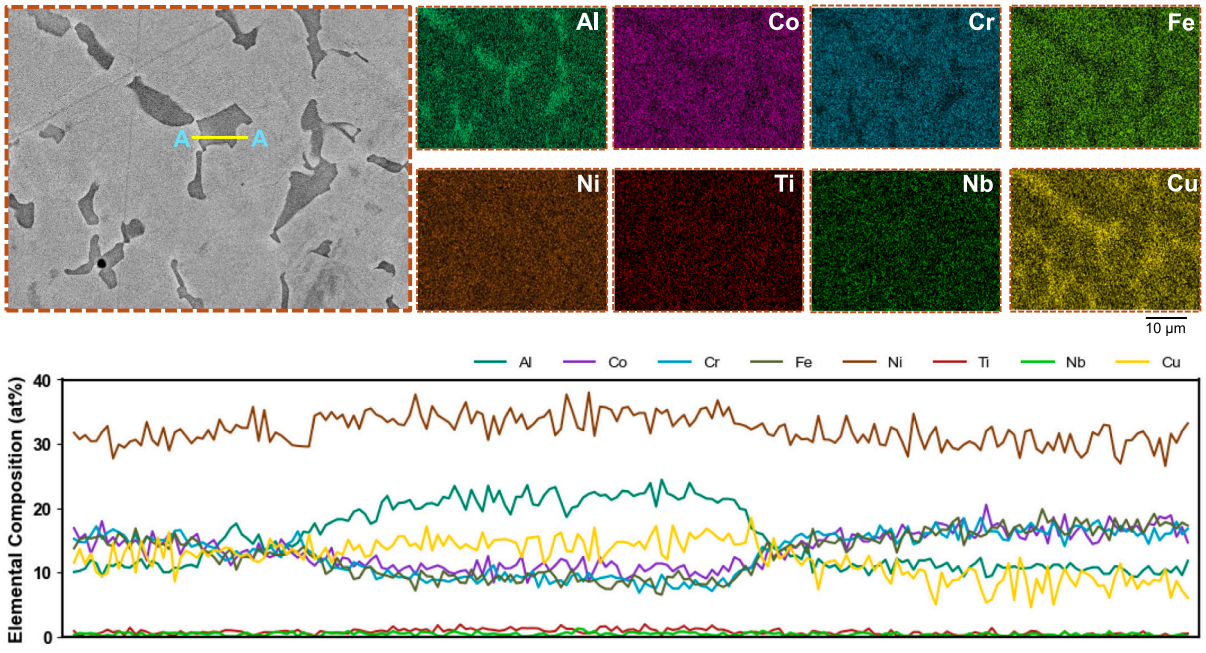

Fig. 6. BSE image of macrosegregated island with elemental mapping.

interdendritic regions are enriched in Cu, Al and Ni, whereas the dendritic cores are enriched in Co, Cr, Fe and Ni. Similar kind of Cu-Al-Ni segregation behaviour has been reported during solid/liquid bonding of Cu with $AlCoCrFeNi_{2.1}$ [65]. Surrounding the islands, columnar dendrites are observed (refer to Fig. 3 (c)) whose growth is promoted by localized thermal gradients between the islands and the surrounding matrix, driving directional solidification.

Finally, at the fusion boundary of both base metals, epitaxial nucleation is observed, a phenomenon commonly reported in fusion welding. Notably, at the $AlCoCrFeNi_{2.1}$ fusion boundary a uniform solidification front is formed, in contrast to the eutectic morphology characteristic of the base metal. These distinct solidification features are attributed to the rapid release of latent heat driven by elemental intermixing, which alters the weld pool chemistry enhancing constitutional undercooling [66]. Similar observations have been reported in studies involving rapid solidification of the $AlCoCrFeNi_{2.1}$ alloy [67]. The grain orientation in these zones aligns perpendicular to the direction of maximum heat extraction or the steepest temperature gradient [68,69].

3.2. Thermodynamic - CALPHAD simulation

Thermodynamic CALPHAD simulations were performed using Thermo-Calc software with TCHEA 5.1 database. The classical Scheil-Gulliver model was employed to predict the non-equilibrium solidification behaviour characteristic of arc-based fusion welding. The model assumes (i) infinitely fast diffusion in liquid phase, (ii) negligible back diffusion in the solid phase and (iii) local equilibrium at the solid-liquid interface. EDS line scan compositions across the joint were used as input data to simulate the spatial evolution of solidus and liquidus temperatures. Fig. 7 shows a strong correlation between Nb enrichment and elevated liquidus temperature, consistent with Nb's role in stabilizing high melting phases such as C14 Laves. With decreasing Ti concentration, the liquidus decreases (direct correlation near the NiTi interface), whereas the solidus rises slightly partially counteracting the melting-point-depressant effect of Cu. A sharp decrease of Nb and Ti is observed toward the weld centre. Contrary, Cu, owing to its high diffusion coefficient, remains uniformly distributed from the weld centre until the $AlCoCrFeNi_{2.1}$ fusion boundary with an average concentration of 12.3 ± 0.8 at.%, resulting in a reduction of the solidus and liquidus temperatures by ≈342 °C and ≈82 °C, relative to the $AlCoCrFeNi_{2.1}$ base metal. Similar Cu-induced reductions in phase formation temperature have been reported in CoCrFeNi HEA alloy [70]. Furthermore, the higher thermal conductivity of NiTi 18–28 W/m.k [60], compared to $AlCoCrFeNi_{2.1}$ of ~10 W/m.k (calculated from Thermo-Calc), sustains steep temperature gradients, enhancing constitutional undercooling and promoting heterogeneous solidification pathways.

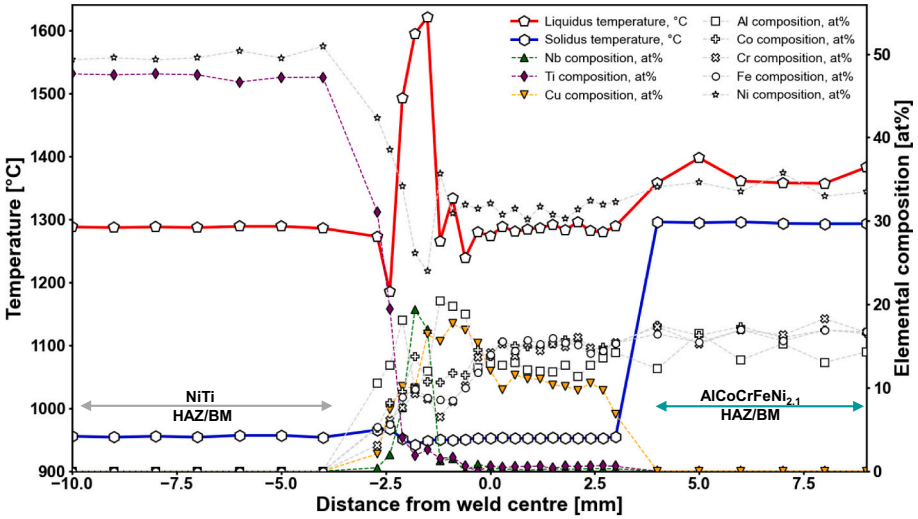

Fig. 7. Scheil solidus and liquidus temperature evolution across the weld zone.

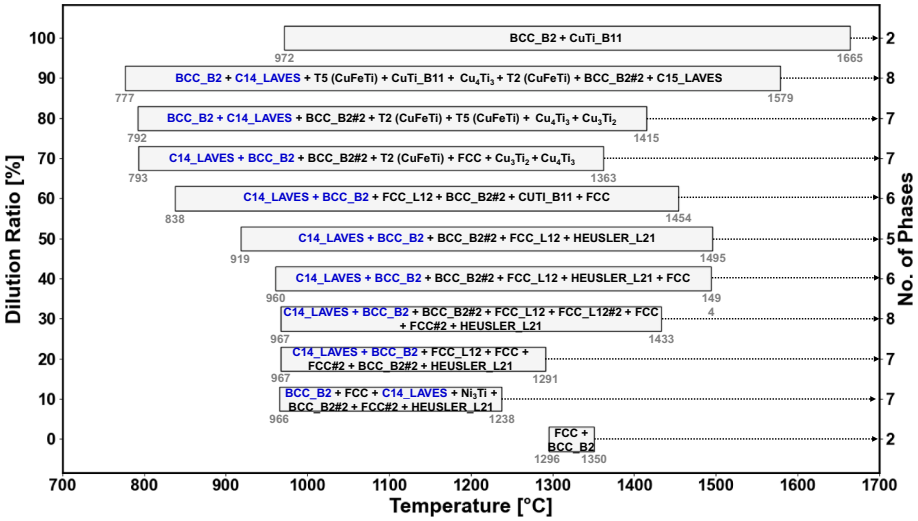

Fig. 8. Phase formation as a function of dilution ratio and solidification range.

Table 4
Enthalpy of mixing (ΔHmix, kJ/mol) for binary elemental pair [75].

Elements	Nb	Ti	Cu	Al	Co	Cr	Fe	Ni
Nb		2	3	−18	−25	−7	−16	−30
Ti			−9	−30	−28	−7	−17	−35
Cu				−1	6	12	13	4
Al					−19	−10	−11	−22
Co						−4	−1	0
Cr							−1	−7
Fe								−2

Fig. 8 illustrates the phase evolution in the $AlCoCrFeNi_{2.1}$ as a function of progressive Nb-Ti-Cu dilution. At 0% dilution, the alloy solidifies as FCC + B2 BCC with a relatively narrow freezing range (54 °C). 100% dilution represents a hypothetical ternary alloy composed solely of Nb, Ti and Cu. C14 Laves and B2 phase (both highlighted in blue color in Fig. 8) persist across all dilution levels, signifying their thermodynamic stability. The FCC is present up to 40% dilution ratio. From 50% dilution up, Cu-rich intermetallics emerge, consistent with equilibria in Cu—Ti and Cu-Fe-Ti systems, reflecting increasing chemical complexity. Cu addition markedly reduces the solidus temperature, widening the solidification interval and promoting multi-stage solidification. The combined presence of high melting point elements such as Nb and Ti, with low melting point Cu thus results in a chemically heterogeneous fusion zone containing multiple coexisting phases. To rationalize these observations, the enthalpy of mixing (ΔH_{mix}) for binary elemental pairs is provided in Table 4. Ti exhibits large negative enthalpy of mixing with Al, Co and Ni favouring the formation of B2 BCC phase. While Nb, in addition to large negative enthalpy of mixing with Co, Fe and Ni also exhibits large atomic size misfit and Allen electronegativity difference with Co, Cr, Fe and Ni as shown in Table 5, promotes the formation of C14 Laves phase [71]. Cu, with its weak negative or positive mixing enthalpies with other elements, is segregated into interdendritic regions. The similar atomic radii and higher valence electron concentration (VEC) of Cu, Co, Cr, Fe and Ni favour FCC solid solution [72,73]. These parameters suggest a competition between C14 Laves and FCC phases, which is corroborated by the coupled eutectic morphology observed in reaction layer II. Similar results were also reported between Fe_2Nb (C14 Laves) and Fe [74].

Cr, Co and Fe are well known sigma phase (σ) forming elements (SFE) and the dissolution of Nb and Al also contributes as an SFE due to established Nb—Al pairing [78]. Despite this, σ phase was not predicted in the Scheil simulation. This absence is expected, since Scheil modelling represents rapid, non-equilibrium solidification and neglects solid state diffusion. σ phase formation in AlCoCrFeNi-based HEA's is well documented as a diffusion-controlled transformation that typically occurs via post-solidification segregation or aging [79]. In addition to ordered and TCP phases, Ti-rich intermetallics also play a significant role in this dissimilar system. The dilution simulations predicted Ni_3Ti in 10% dilution range consistent with the Ni—Ti binary phase diagram. However low temperature and metastable Ni—Ti intermetallics were not predicted. Their experimental detection suggests that elemental intersolubility dynamically modifies weld pool chemistry, producing chemically graded zones. These gradients influence local solidification pathways by inducing constitutional undercooling and altering latent heat extraction.

3.3. High energy synchrotron X-ray diffraction

The complex phase evolution and transformations across the weld zone were systematically investigated using high-intensity synchrotron X-ray diffraction in transmission mode setup. The superior brilliance, photon flux and monochromatic nature of synchrotron radiation enable the detection of minor and nanoscale phases that are often indiscernible using conventional (i.e., laboratorial) diffraction methods due to their resolution limitations. Fig. 9 presents the 2D gaussian-smoothened phase maps acquired across the entire weld zone, encompassing both base metals. Each phase identified from the diffractograms is plotted separately for clarity: the B2 austenitic phases of NiTi and B2 BCC phase of $AlCoCrFeNi_{2.1}$ in Fig. 9 (a); the FCC phase in Fig. 9 (b); the ordered $L1_2$ FCC phase in Fig. 9 (c); and the topologically close-packed σ and C14 Laves phases in Fig. 9 (e) and (f), respectively. These maps incorporate both the normalized integrated intensity and the peak broadening (FWHM) of selected reflections, thereby enabling visualization of spatial phase evolution under the non-uniform weld thermal cycle. The Ti-rich segregations previously observed in the BSE micrographs in Fig. 5, are here identified as Ti_2Ni and Ti_2Cu, shown in Fig. 9 (g) and (h) confirming co-localization of Ni and Cu with Ti. The enrichment of TCP and Ti-rich intermetallic compounds in the narrow region near the NiTi interface arises from compositional gradients generated by elemental intersolubility. These gradients increase the degree of constitutional undercooling during solidification, which in turn restricts the nucleation and growth of these intermetallic compounds to this localized region. The results are consistent with thermodynamic phase predictions discussed earlier.

Fig. 10 presents the root-mean-square error (RMSE) of the 2θ variation across the weld zone, serving the dual purpose of confirming the reliability of phase-indexing and quantifying lattice distortion. This approach is especially relevant due to the multiphase nature of the regions that compose the welded joint compounded by the low volume fraction of low symmetry phases that can also exist. Fig. 11 shows the normalized intensity and full width half maximum (FWHM) of representative reflections to assess phase transformations under the influence of weld thermal cycle. Reflections were chosen based on structural significance and minimal overlap with others such as, B2 (110) for its high multiplicity and strain sensitivity, FCC (200) for its resistance to stacking fault and twinning effects, $L1_2$ (100) and σ (101) as principal reflections, and non-overlapping peaks for C14, Ti_2Ni and Ti_2Cu to minimize convolution effects and ensure reliable evaluation of peak position and broadening.

Both the base metals NiTi and $AlCoCrFeNi_{2.1}$, exhibit the lowest RMSE $<0.01°$ indicating well-ordered lattices with minimal microstrain. Moving into the heat affected regions, a differential phase evolution becomes evident. On the NiTi side, a reduction in RMSE accompanied by

Table 5
Atomic radii, Allen electronegativity and VEC of constituent elements [73,76,77].

Parameter	Nb	Ti	Cu	Al	Co	Cr	Fe	Ni
Atomic radii (Å)	1.429	1.462	1.278	1.432	1.251	1.249	1.241	1.246
Allen electronegativity ($\Delta\chi_{allen}$)	1.41	1.38	1.85	1.613	1.84	1.65	1.80	1.88
Valence electron concentration	5	4	11	3	9	6	8	10

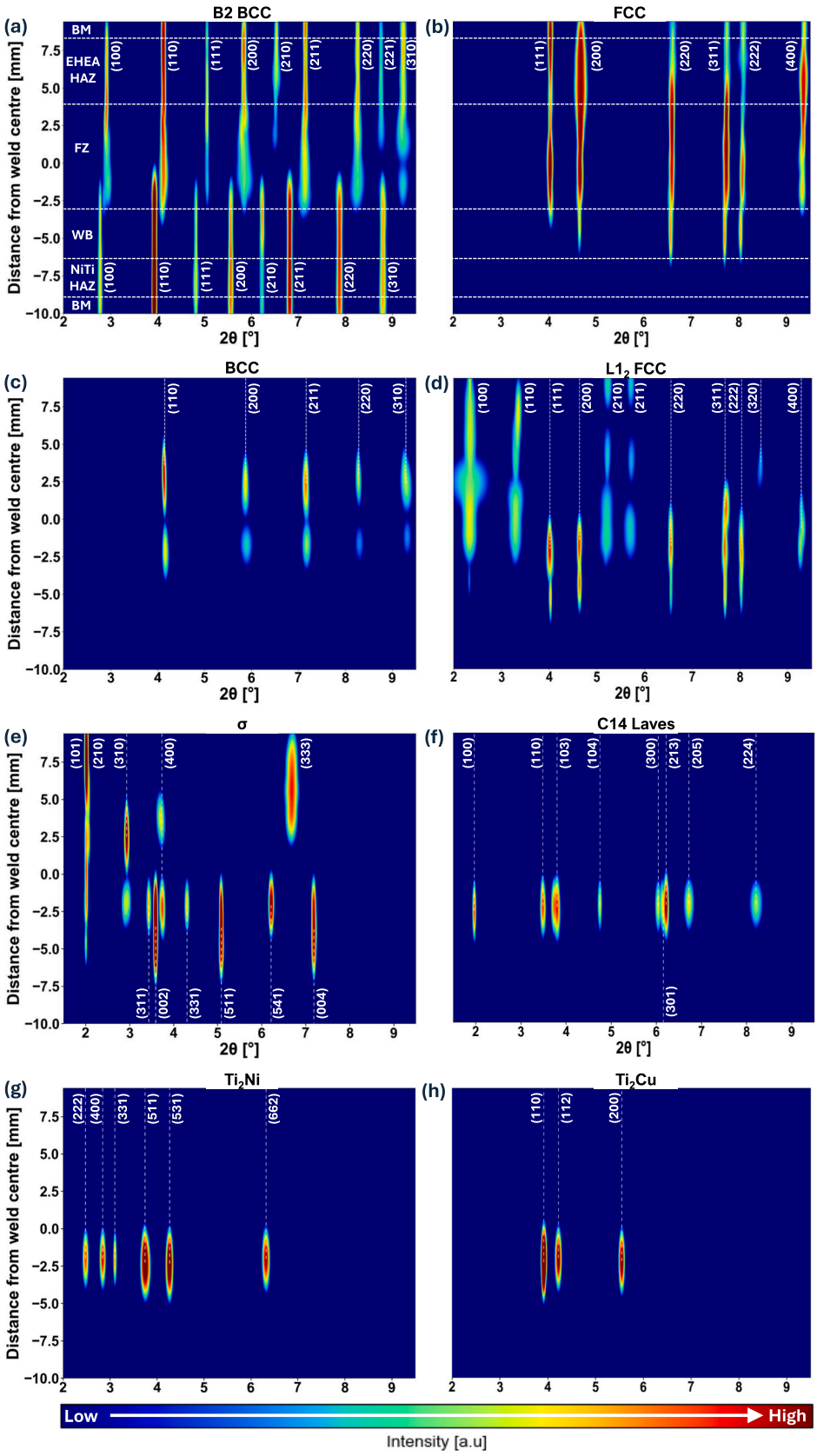

Fig. 9. 2D Gaussian-smoothed SXRD phase evolution maps across the weld zone. a) B2, b) disordered FCC, c) BCC, d) $L1_2$, e) σ, f) C14 Laves, g) Ti_2Ni and h) Ti_2Cu.

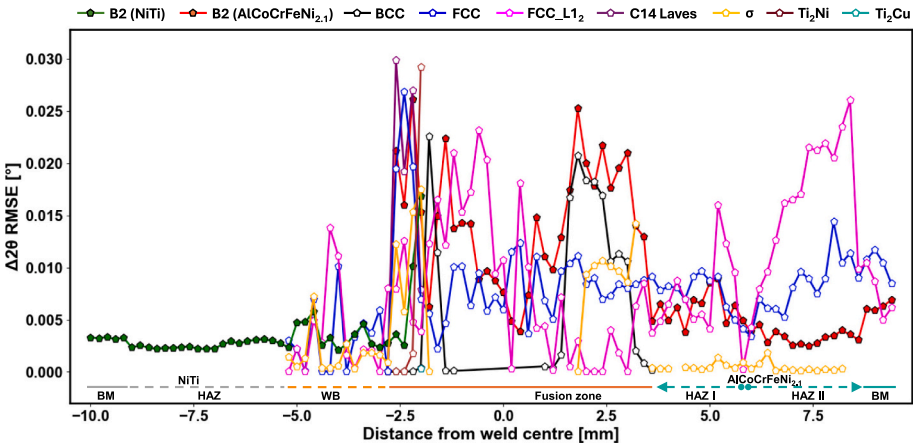

Fig. 10. RMSE variation across the weld zone.

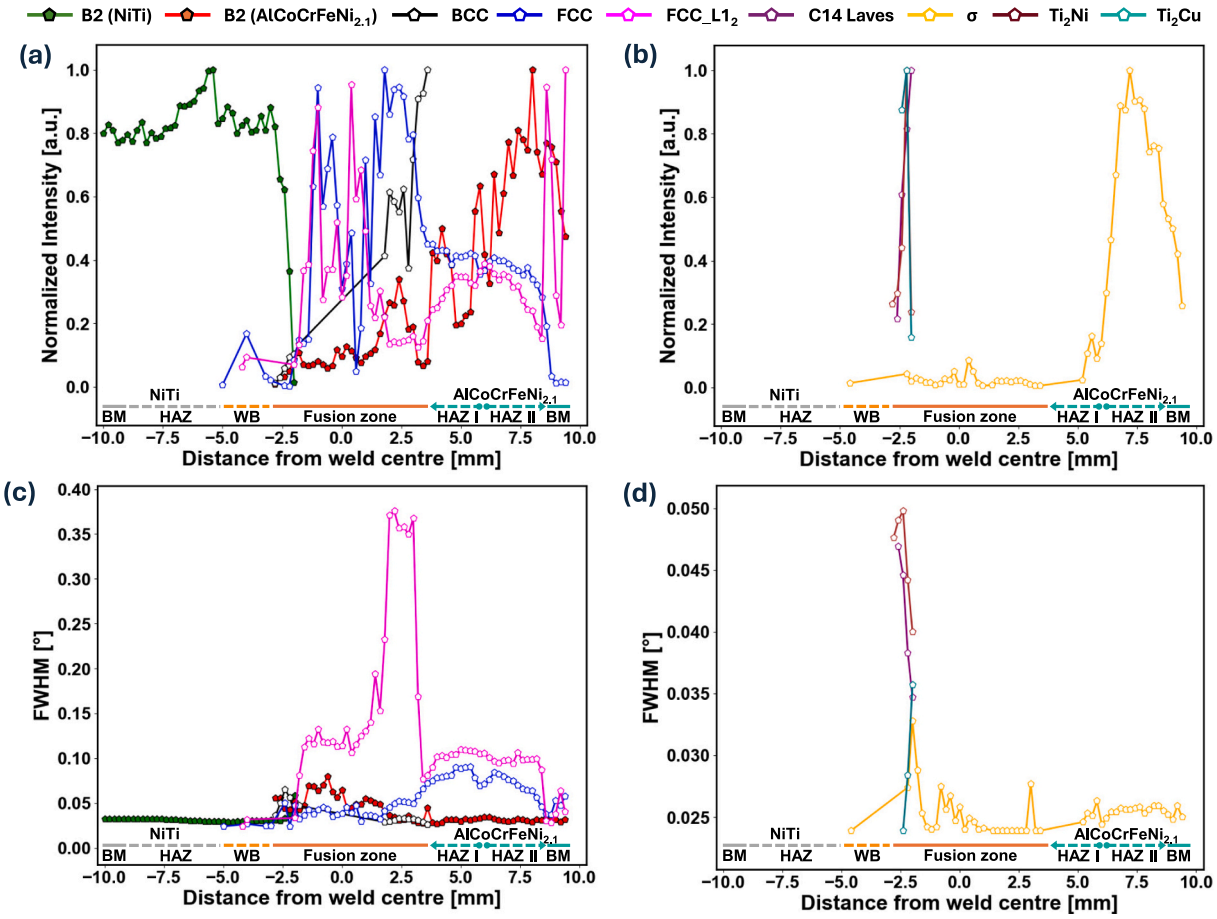

Fig. 11. Normalized intensity and FWHM variation of representative peaks across the weld zone. a) B2, FCC, $L1_2$ and BCC b) C14, σ, Ti_2Ni and Ti_2Cu. FWHM evolution across the weld zone c) B2, FCC, $L1_2$ and BCC d) C14, σ, Ti_2Ni and Ti_2Cu.

an increase in intensity and FWHM narrowing indicates stress relaxation of the cold-worked matrix, attributed to reduced thermal exposure enabled by AOW configuration and multi-interlayer shielding. On the $AlCoCrFeNi_{2.1}$ side, two distinct sub-zones are identified. The FCC (200) and (400) non-close packed reflections, highly sensitive to lattice strains, exhibit peak broadening across both HAZ I and HAZ II, as shown in Fig. 9 (b) Fig. 10 (c). The outer zone adjacent to BM, designated as HAZ II, experiences the lowest thermal gradient. Here, the B2 phase exhibits the modest RMSE reduction, while the σ phase shows no change. In contrast, the $L1_2$ nanoprecipitates exhibit RMSE spikes accompanied by notable FWHM broadening, reflecting thermal strain redistribution from the ordered B2 and σ phases to the surrounding FCC and $L1_2$ phases. The inner zone adjacent to the fusion boundary, designated as HAZ I, experiences a significantly higher thermal gradient. In this region, attenuation of the close-packed FCC (111) and (222) reflections implies dislocation annihilation and sub-grain recovery, while enhancement of the intermediate (220) and (311) reflections with concurrent FWHM reduction indicates recrystallization and stress relief. The appearance of (210) and (211) new $L1_2$ reflections, absent in the base metal, further corroborates thermally activated recrystallization.

Unlike the other phases that exhibit lattice relaxation and recovery, the σ phase displays a stable Δ2θ° coupled with a simultaneous reduction in intensity and FWHM. This behaviour indicates the dissolution of highly strained σ domains and consequent strain localization at σ/matrix interfaces under elevated thermal gradients. This distinct behaviour arises from the limited plasticity of tetragonal σ phase, which possess few slip systems compared to cubic structures. Thus, while HAZ II primarily exhibits strain redistribution and partial recovery, HAZ I transitions to recrystallization and strain localization.

Across the fusion zone, the multiphase transformation during resolidification is distinctly non-uniform as evident in Fig. 9, Fig. 10 and Fig. 11. In the regions adjacent to NiTi and $AlCoCrFeNi_{2.1}$ interfaces, the B2($AlCoCrFeNi_{2.1}$) accommodates substantial thermal strain, manifested as a pronounced RMSE variation and a clear 2θ offset between the B2 and its overlapping BCC component, previously indiscernible in the BM and HAZ. Within the fusion zone (except the NiTi interface) FCC phase remains comparatively stable, showing minimal RMSE variation of ±0.007° and narrow FWHM, consistent with Cu dissolution from the interlayer, which enhances FCC stabilization. Conversely the $L1_2$ phase exhibits opposing trends. In the fusion zone near the NiTi interface, $L1_2$ shows higher RMSE and intensity with FWHM comparable to HAZ, likely driven by Ni enrichment from NiTi BM. Toward $AlCoCrFeNi_{2.1}$ BM, the $L1_2$ intensity decreases sharply (lowest across the weld zone) while FWHM broadens significantly up to 0.376°, indicating severe lattice strain accumulation. For all the phases at the NiTi interface high thermal strain combined with enhanced elemental intersolubility results in markedly elevated RMSE values. This is accompanied by the formation of additional phases such as C14 Laves and Ti-rich intermetallic compounds, and also reinforcing the σ phase.

After analysing the peak fitted parameters, the Williamson-Hall (W—H) method was applied to evaluate the phase-specific strain partitioning, as well as the evolution of microstrain (με) and crystallite size (D) across the heterogeneous weld zone. A minimum of three reflections per phase were used to ensure statistical reliability. The matrix phases are presented in Fig. 12 (a) and (b), while the intermetallic compounds are presented separately in Fig. 12 (c) and (d). On the NiTi side, the HAZ exhibits pronounced peak sharpening and reduced microstrain, confirming stress relaxation of the cold-worked structure. On the AlCoCrFeNi$_{2.1}$ side, the B2 phase displays stress relaxation in HAZ II, whereas in HAZ I, microstrain increase in B2 is counterbalanced by the FCC and $L1_2$ phases, consistent with earlier FWHM and RMSE trends. Within the fusion zone, B2 and BCC phases exhibit a steep increase in microstrain indicating enhanced lattice distortion under steep thermal gradients during welding. In addition a marked increase in crystallite size is observed along the fusion boundaries (or) interfaces, which is attributed to longer thermal residence times and slower cooling rates in these regions promoting coarsening of the diffracting domains. At the NiTi interface the crystallite size increases even further. Here the higher thermal conductivity of NiTi enhances the heat extraction rate (which increases local thermal residence time) resulting in the formation of larger coherent diffracting domains. Notably, the FCC phase exhibits the lowest microstrain across the fusion zone. This reduction can be attributed to Cu dissolution in the disordered FCC matrix. As discussed in Section 3.2, Cu has an comparable atomic radius and higher VEC with other FCC forming elements, which promotes a compositionally homogeneous solid solution. Such homogenization reduces lattice distortion, thereby reducing the internal strain with the FCC grains. In contrast, the $L1_2$ phase displays the highest compressive strain. This arises from the

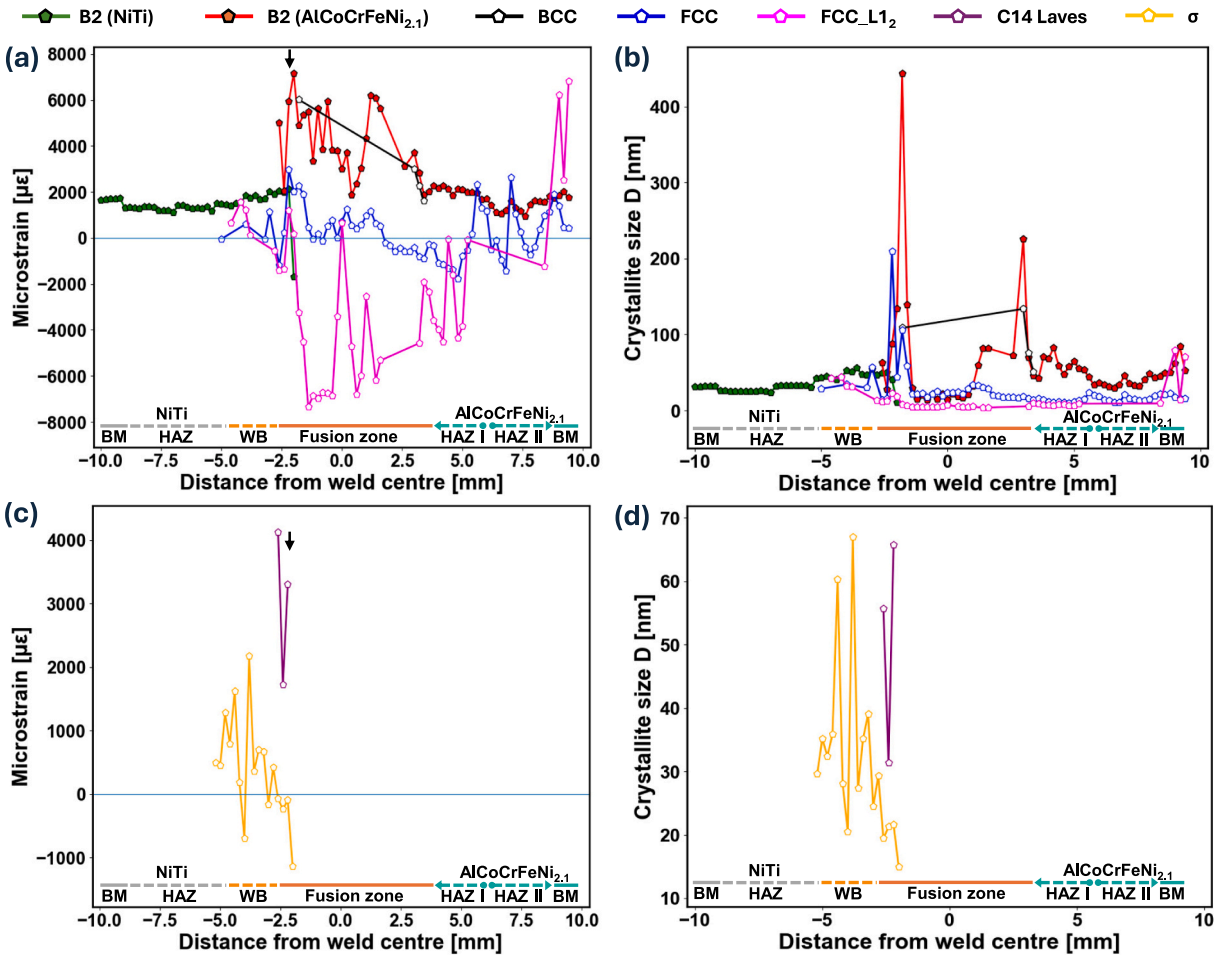

Fig. 12. Microstrain and crystallite size evolution across weld zone employing Williamson-Hall analysis.

coherent lattice coupling between the $L1_2$ precipitates and the surrounding FCC matrix. This lattice mismatch across the coherent FCC-$L1_2$ interface generates elastic strain energy. While the disordered FCC matrix can partially accommodate this strain through local atomic distortions and defects formation, the ordered $L1_2$ has limited capacity for plastic relaxation because the dislocation motion would disrupt the long-range atomic ordering. Consequently a greater fraction of this mismatch strain is stored as the elastic strain within the $L1_2$ domains, leading to the comparatively higher compressive microstrain observed for this phase. These observations suggests that the weld ordered phases predominantly experience tensile microstrain, while the ductile FCC phase accommodates compressive strain, reflecting strain partitioning among coexisting phases. At the NiTi interface, all phases collectively contribute to tensile strain (as indicated by arrows in Microstrain and crystallite size evolution across weld zone employing Williamson-Hall analysis. (a) and (b)), while the adjacent braze weld region exhibits compressive strain. This steep tensile-compressive gradient cannot be plastically accommodated due to the enrichment in brittle and ordered phases. Consequently, the mismatch amplifies local stress fields generating stress triaxiality that promotes crack initiation and propagation [80]. Overall, these synchrotron results elucidate coupled phase evolution and microstrain governed by combined influence of compositional heterogeneity and thermal gradients across the dissimilar weld.

3.4. Tensile and microhardness analysis

Fig. 13, illustrates the non-uniform hardness distribution across the weld zone consistent with the heterogeneous microstructure and complex phase evolution discussed before. The NiTi base metal, exhibits a higher microhardness of ≈405 $HV_{0.3}$ attributed to its cold worked polycrystalline microstructure. This value decreases to ≈338 $HV_{0.3}$ in the HAZ, due to grain coarsening and the corresponding reduction in the grain boundary area in agreement with the Hall-Petch relationship. Although the multi-interlayer shielding limited thermal exposure of the NiTi base metal, its high thermal conductivity promoted rapid heat extraction, leading to a relatively wider HAZ compared to AlCoCrFeNi$_{2.1}$side. The region extending from NiTi interface to weld centre, exhibits an exceptional peak hardness of 856 $HV_{0.3}$, consistent with the presence of TCP and Ti-rich intermetallics, as confirmed by SXRD. By contrast, the region from the weld centre to AlCoCrFeNi$_{2.1}$ interface shows a significantly lower hardness of ≈373 $HV_{0.3}$. This disparity is attributed to enhanced Cu diffusion, which stabilizes ductile and softer FCC phase. The AlCoCrFeNi$_{2.1}$ HAZ and BM exhibits a minor hardness difference (≈5 $HV_{0.3}$), confirming that the rapid heat extraction through NiTi preserved the microstructural stability of AlCoCrFeNi$_{2.1}$. However it could be observed that the hardness is distributed uniformly in HAZ II relative to HAZ I due to the lattice relaxation and strain partitioning among phases as discussed earlier in SXRD analysis.

Table 6 summarizes the tensile properties of the base metals and interlayers. Notably, the AlCoCrFeNi$_{2.1}$ alloy exhibits higher fracture strain compared to NiTi, owing to its alternating lamellar morphology that mitigates the strength-ductility trade-off. NiTi shows a characteristic stress plateau (SP). The dissimilar weld joint fractured at an ultimate tensile strength of 372 MPa and a fracture strain of 1.11%, indicating brittle behaviour. This suggests that as the fusion zone approached the yield strength (transition from elastic to plastic deformation) of the AlCoCrFeNi$_{2.1}$ base metal, stress localizes in the regions of elevated hardness comprising the TCP and Ti-rich intermetallics compounds. The limited slip systems and high lattice rigidity of these phases reduce their ability to accommodate plastic deformation, thereby promoting crack initiation and fracture in these hardened zones. Fig. 14 presents SEM fractographs of the fracture surfaces. The region adjacent to NiTi interface as shown in Fig. 14 (a), exhibits cleavage facets, facet steps, river patterns and secondary cracks confirming brittle cleavage fracture. This brittle behaviour correlates with the enrichment of TCP and Ti_2Ni, which act as crack initiation site. In contrast, the region adjacent to fusion zone as shown in Fig. 14 (b), exhibits micro-dimples formed by micro-void coalescence along with shear lips, indicative of ductile tearing. These observations confirm a mixed-mode fracture mechanism, with crack initiation occurring in the embrittled NiTi interface region followed by partial ductile tearing toward the fusion

Table 6
Tensile properties of base metals and interlayers.

Base metal	Yield strength (MPa)	Ultimate tensile strength (MPa)	Elongation %
NiTi	~400 (Superelastic plateau)	1150	22.0
Nb interlayer	240	585	5.0
Cu interlayer	270	314	14.0
AlCoCrFeNi$_{2.1}$	284	1039	20.6

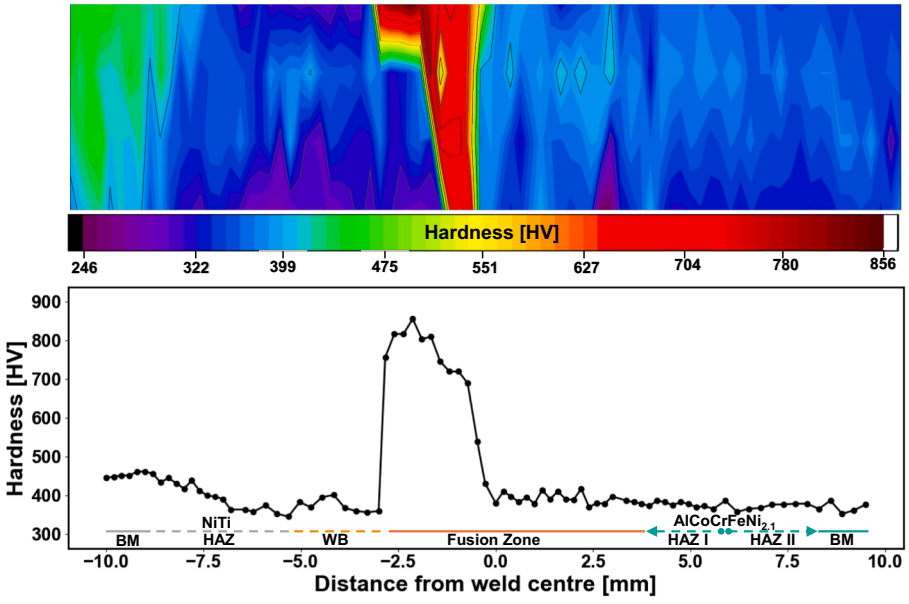

Fig. 13. Vickers microhardness contour plot with corresponding line hardness profile across the weld zone.

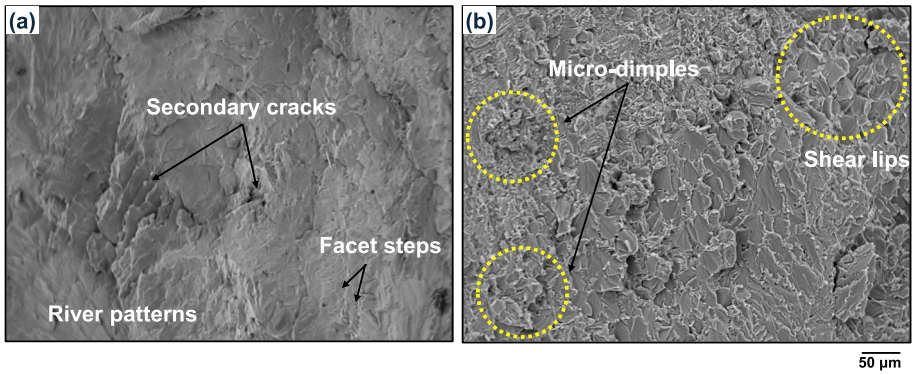

Fig. 14. SEM fractography of the fractured weld joint, (a) region adjacent to NiTi interface and (b) region adjacent to fusion zone.

zone.

Although the joint efficiency is significantly lower than that of the base metals and interlayers, it is noteworthy that preliminary trials without interlayers resulted in catastrophic cracking even before specimen removal from the weld fixture. While the present multi-interlayer strategy results in limited tensile ductility, it successfully confines embrittlement to a much narrower region in the fusion zone due to the chemically induced constitutional undercooling.

4. Conclusions

This study investigates the dissimilar joining of NiTi shape memory and $AlCoCrFeNi_{2.1}$ eutectic high entropy alloy using a multi-interlayer strategy, revealing significant microstructural heterogeneity and phase evolution across the composite weld zone.

1. Arc offset welding, facilitated a weld-brazing joint at the NiTi interface, and dissolution of Nb and Cu interlayers promoted elemental intermixing, resulting in the formation of multiple reaction layers and macrosegregated islands.
2. Nb promoted the formation of C14 Laves due to its atomic size misfit and allen electronegativity mismatch, while Ti preferentially stabilizes B2 solid solution, also promotes Ti rich intermetallics. Cu enhances the stabilization of the FCC solid solution, acting as a melting point depressant, and widened the solidification interval. The resulting heterogeneous chemical distribution, combined with intrinsic thermal conductivity mismatch of the base metals, produced a spatially non-uniform microstructure across the fusion zone.
3. Phase evolution observed in the composite weld zone was confirmed by synchrotron X-ray diffraction analysis, which closely matches CALPHAD simulation, indicating that elemental intermixing and the transient weld thermal cycle govern the solidification pathway and phase stability.
4. Mechanical characterization showed that the NiTi interfacial region exhibited the highest hardness due to enrichment of TCP phases and Ti_2Ni intermetallics. Cracks initiated in this hardened region, resulting in cleavage-dominated fracture during tensile testing. Although the ultimate tensile strength was significantly lower than that of either base metal, the multi-interlayer configuration produced weld joint and successfully confined embrittlement to a narrow region in the fusion zone.

Based on these findings, future work will focus on optimizing interlayer chemistry, thickness, and welding parameters to suppress TCP phase formation and improve joint efficiency toward levels comparable to the base metals.

CRediT authorship contribution statement

Nithin Joseph Reddy Sagili Arthur: Writing – original draft, Visualization, Validation, Software, Methodology, Investigation, Formal analysis, Data curation. **Rae Eon Kim:** Methodology, Investigation. **Ana Martins:** Investigation, Data curation. **Hyoung Seop Kim:** Validation, Methodology. **N. Schell:** Validation, Resources. **João Pedro Oliveira:** Writing – review & editing, Supervision, Project administration.

Funding

Nithin Joseph Reddy Sagili Arthur, acknowledges funding from Fundação para a Ciência e a Tecnologia (FCT) for its financial support via the PhD grant 2022.10356.BD. The authors acknowledges funding by national funds from FCT - Fundação para a Ciência e a Tecnologia, I. P., in the scope of the projects LA/P/0037/2020, UIDP/50025/2020 and UIDB/50025/2020 of the Associate Laboratory Institute of Nanostructures, Nanomodelling and Nanofabrication – i3N. We acknowledge DESY (Hamburg, Germany), a member of the Helmholtz Association HGF, for the provision of experimental facilities. Parts of this research were carried out at P07 The High Energy Materials Science Beamline of Helmholtz-Zentrum Hereon and DESY. Data was collected using P07 beamline operated/provided by Helmholtz-Zentrum Hereon. Beamtime was allocated for proposal I-20241103 EC.

Declaration of competing interest

The authors declare that they have no known competing financial interests or personal relationships that could have appeared to influence the work reported in this paper.

Appendix A. Supplementary data

Supplementary data to this article can be found online at https://doi.org/10.1016/j.matchar.2026.116267.

Data availability

All data generated or analysed during this study are included in this published article.

References

[1] J.P. Bergmann, R. Schuerer, K. Ritter, Friction stir welding of tailored blanks of aluminum and magnesium alloys, in: Key Eng Mater, Trans Tech Publications Ltd, 2013, pp. 492–499, https://doi.org/10.4028/www.scientific.net/KEM.549.492.
[2] S. Ganguly, Welding of dissimilar metals, in: Welding of Metallic Materials: Methods, Metallurgy, and Performance, 2023, pp. 317–365, https://doi.org/10.1016/B978-0-323-90552-7.00014-6.
[3] S. Meco, G. Pardal, S. Ganguly, S. Williams, N. McPherson, Application of laser in seam welding of dissimilar steel to aluminium joints for thick structural

components, Opt. Lasers Eng. 67 (2015) 22–30, https://doi.org/10.1016/j.optlaseng.2014.10.006.
[4] H.C. Chen, A.J. Pinkerton, L. Li, Fibre laser welding of dissimilar alloys of Ti-6Al-4V and Inconel 718 for aerospace applications, Int. J. Adv. Manuf. Technol. 52 (2011) 977–987, https://doi.org/10.1007/s00170-010-2791-3.
[5] Welding Metallurgy Principles, in: Welding Metallurgy and Weldability, 2015, pp. 9–83, https://doi.org/10.1002/9781118960332.ch2.
[6] R.W. Messler, Joining of metals, alloys, and Intermetallics, in: Joining of Materials and Structures, 2004, pp. 535–582, https://doi.org/10.1016/B978-075067757-8/50011-7.
[7] D.C. Lagoudas, Shape Memory Alloys : Modeling and Engineering Applications, Springer, 2008, https://doi.org/10.1007/978-0-387-47685-8.
[8] D.J. Hartl, D.C. Lagoudas, Aerospace applications of shape memory alloys, proc Inst mech Eng G, J. Aerosp. Eng. 221 (2007) 535–552, https://doi.org/10.1243/09544100JAERO211.
[9] A. Concilio, V. Antonucci, F. Auricchio, L. Lecce, E. Sacco, Shape Memory Alloy Engineering: for Aerospace, Structural, and Biomedical Applications, Elsevier, 2021, https://doi.org/10.1016/B978-0-12-819264-1.01001-3.
[10] K. Otsuka, X. Ren, Physical metallurgy of Ti-Ni-based shape memory alloys, Prog. Mater. Sci. 50 (2005) 511–678, https://doi.org/10.1016/j.pmatsci.2004.10.001.
[11] H. Vashishtha, J. Jain, Influence of laser power on precipitate formation and multiple step transformation kinetics in NiTi shape memory alloy weld joints, J. Alloys Compd. 893 (2022), https://doi.org/10.1016/j.jallcom.2021.162307.
[12] J. Liu, G. Chen, H. Cao, Q. Yin, S. Yu, B. Zhang, J. Cao, Y. Huang, Mechanical and functional properties degradation mechanism of electron beam welded NiTi shape memory alloy, Vacuum 198 (2022), https://doi.org/10.1016/j.vacuum.2022.110870.
[13] A. Shamsolhodaei, M.H. Razmpoosh, C. Maletta, P. Magaro, Y.N. Zhou, A comprehensive insight into the superelasticity measurement of laser welded NiTi shape memory alloys, Mater. Lett. 287 (2021), https://doi.org/10.1016/j.matlet.2021.129310.
[14] G. Chen, J. Liu, Z. Dong, Y. Li, Y. Zhao, B. Zhang, J. Cao, Understanding mechanisms of shape memory function deterioration for nitinol alloy during non-equilibrium solidification by electron beam, J. Adv. Res. 33 (2021) 99–108, https://doi.org/10.1016/j.jare.2021.02.007.
[15] S. Asadi, T. Saeid, Y. Kim, F. Habibi, M. Hyeon Jang, A. Sugiarto, A. Valanezhad, N. Park, Microstructural evolution in the heat-affected zone of laser-welded superelastic NiTi alloy wire, Mater. Lett. 304 (2021), https://doi.org/10.1016/j.matlet.2021.130606.
[16] S. Datta, M.S. Raza, P. Saha, D.K. Pratihar, Study on mechanical performance of laser-welded NiTinol sheet, Proc. Inst. Mech. Eng. B J. Eng. Manuf. 237 (2023) 2073–2084, https://doi.org/10.1177/0954405420937532.
[17] H.M. Li, D.Q. Sun, X.L. Cai, P. Dong, W.Q. Wang, Laser welding of TiNi shape memory alloy and stainless steel using Ni interlayer, Mater. Des. 39 (2012) 285–293, https://doi.org/10.1016/j.matdes.2012.02.031.
[18] H. Li, D. Sun, X. Cai, P. Dong, X. Gu, Laser welding of TiNi shape memory alloy and stainless steel using co filler metal, Opt. Laser Technol. 45 (2013) 453–460, https://doi.org/10.1016/j.optlastec.2012.06.010.
[19] H. Li, D. Sun, X. Gu, P. Dong, Z. Lv, Effects of the thickness of cu filler metal on the microstructure and properties of laser-welded TiNi alloy and stainless steel joint, Mater. Des. 50 (2013) 342–350, https://doi.org/10.1016/j.matdes.2013.03.014.
[20] A. Shojaei Zoeram, S.A.A. Akbari Mousavi, Effect of interlayer thickness on microstructure and mechanical properties of as welded Ti6Al4V/cu/NiTi joints, Mater. Lett. 133 (2014) 5–8, https://doi.org/10.1016/j.matlet.2014.06.141.
[21] A. Shojaei Zoeram, S.A.A. Akbari Mousavi, Laser welding of Ti-6Al-4V to nitinol, Mater. Des. 61 (2014) 185–190, https://doi.org/10.1016/j.matdes.2014.04.078.
[22] J.P. Oliveira, B. Panton, Z. Zeng, C.M. Andrei, Y. Zhou, R.M. Miranda, F.M. B. Fernandes, Laser joining of NiTi to Ti6Al4V using a niobium interlayer, Acta Mater. 105 (2016) 9–15, https://doi.org/10.1016/j.actamat.2015.12.021.
[23] A. Shojaei Zoeram, A. Rahmani, S.A.A. Akbari Mousavi, Microstructure and properties analysis of laser-welded Ni–Ti and 316l sheets using copper interlayer, J. Manuf. Process. 26 (2017) 355–363, https://doi.org/10.1016/j.jmapro.2017.02.005.
[24] X.L. Gao, X.Q. Wang, J. Liu, L. kun Li, A novel laser welding method for the reliable joining of NiTi/301SS, Mater. Lett. 268 (2020), https://doi.org/10.1016/j.matlet.2020.127573.
[25] S. Chatterjee, S.S. Mahapatra, K.S. Arora, A. Behera, Physical and mechanical characterization of dissimilar laser welded joints of AISI 316/cu/SMA using fiber laser technology, J. Laser Appl. 32 (2020), https://doi.org/10.2351/7.0000003.
[26] A. Shamsolhodaei, J.P. Oliveira, N. Schell, E. Maawad, B. Panton, Y.N. Zhou, Controlling intermetallic compounds formation during laser welding of NiTi to 316L stainless steel, Intermetallics 116 (2020), https://doi.org/10.1016/j.intermet.2019.106656.
[27] F. Ge, B. Peng, J.P. Oliveira, W. Ke, F.B. Teshome, Y. Li, Z. Zeng, Dissimilar laser welding of a NiTi shape memory alloy to Ti2AlNb, Metals (Basel) 11 (2021), https://doi.org/10.3390/met11101578.
[28] F.B. Teshome, B. Peng, W. Ke, F. Ge, X. Du, Z. Zeng, Prediction of weld Pool profile of dissimilar laser weld between NiTi/Ti6Al4V via different interlayers, in: Proceedings - 2021 7th International Conference on Mechanical Engineering and Automation, ICMEAS 2021, Institute of Electrical and Electronics Engineers Inc, 2021, pp. 107–112, https://doi.org/10.1109/ICMEAS54189.2021.00031.
[29] Yan Zhang, et al., Microstructure and mechanical property improvement of dissimilar metal joints for TC4 Ti alloy to nitinol NiTi alloy by laser welding, Int. J. Mater. Res. 112 (2021) 223–232.
[30] F.B. Teshome, B. Peng, J.P. Oliveira, S. Ao, W. Ke, F. Ge, Z. Zeng, Microstructure, macrosegregation, and mechanical properties of NiTi to Ti6Al4V dissimilar laser welds using co interlayer, J. Mater. Eng. Perform. 31 (2022) 9777–9790, https://doi.org/10.1007/s11665-022-07064-0.
[31] M. Wiegand, N. Sommer, L. Marks, S. Böhm, High-strength dissimilar welds between a NiTi shape memory alloy and titanium obtained by intermixing niobium using pulsed laser beam welding, Metall. Mater. Trans. A Phys. Metall. Mater. Sci. 55 (2024) 278–290, https://doi.org/10.1007/s11661-023-07248-w.
[32] M. Wiegand, L. Marks, N. Sommer, S. Böhm, Dissimilar micro beam welding of titanium to nitinol and stainless steel using biocompatible filler materials for medical applications, Weld. World 67 (2023) 77–88, https://doi.org/10.1007/s40194-022-01412-3.
[33] F.B. Teshome, B. Peng, J.P. Oliveira, Z. Zeng, Dissimilar laser welding of NiTi to Ti6Al4V via Zr interlayer, Mater. Manuf. Process. 38 (2023) 461–470, https://doi.org/10.1080/10426914.2022.2089897.
[34] F.B. Teshome, B. Peng, J.P. Oliveira, J. Shen, S. Ao, H. Li, L. Chen, C. Tan, X. Song, N. Zhou, Z. Zeng, Role of pd interlayer on NiTi to Ti6Al4V laser welded joints: microstructural evolution and strengthening mechanisms, Mater. Des. 228 (2023), https://doi.org/10.1016/j.matdes.2023.111845.
[35] J.W. Yeh, S.K. Chen, S.J. Lin, J.Y. Gan, T.S. Chin, T.T. Shun, C.H. Tsau, S.Y. Chang, Nanostructured high-entropy alloys with multiple principal elements: novel alloy design concepts and outcomes, Adv. Eng. Mater. 6 (2004) 299–303, https://doi.org/10.1002/adem.200300567.
[36] B. Cantor, I.T.H. Chang, P. Knight, A.J.B. Vincent, Microstructural development in equiatomic multicomponent alloys, Mater. Sci. Eng. A 375–377 (2004) 213–218, https://doi.org/10.1016/j.msea.2003.10.257.
[37] Y. Lu, Y. Dong, S. Guo, L. Jiang, H. Kang, T. Wang, B. Wen, Z. Wang, J. Jie, Z. Cao, H. Ruan, T. Li, A promising new class of high-temperature alloys: eutectic high-entropy alloys, Sci. Rep. 4 (2014), https://doi.org/10.1038/srep06200.
[38] Y. Lu, Y. Dong, H. Jiang, Z. Wang, Z. Cao, S. Guo, T. Wang, T. Li, P.K. Liaw, Promising properties and future trend of eutectic high entropy alloys, Scr. Mater. 187 (2020) 202–209, https://doi.org/10.1016/j.scriptamat.2020.06.022.
[39] J. Liu, Z. Li, D. Lin, Z. Tang, X. Song, P. He, S. Zhang, H. Bian, W. Fu, Y. Song, Eutectic high-entropy alloys and their applications in materials processing engineering: a review, J. Mater. Sci. Technol. 189 (2024) 211–246, https://doi.org/10.1016/j.jmst.2023.10.057.
[40] G. Talluri, R.S. Maurya, B.S. Murty, Composition design of eutectic high-entropy alloys: a review, J. Mater. Sci. (2024), https://doi.org/10.1007/s10853-024-10251-0.
[41] M. Zhang, D. Wang, L. He, X. Ye, W. Zhang, Laser beam welding of AlCoCrFeNi2.1 eutectic high-entropy alloy, Mater. Lett. 308 (2022), https://doi.org/10.1016/j.matlet.2021.131137.
[42] J. Shen, P. Agrawal, T.A. Rodrigues, J.G. Lopes, N. Schell, Z. Zeng, R.S. Mishra, J. P. Oliveira, Gas tungsten arc welding of as-cast AlCoCrFeNi2.1 eutectic high entropy alloy, Mater. Des. 223 (2022), https://doi.org/10.1016/j.matdes.2022.111176.
[43] J. Yang, D. Feng, Y. Liu, W. Zheng, S. Lai, D. Yan, Y. He, J. Xie, Excellent corrosion resistance of electron beam welded joint and remelted layer of eutectic high-entropy alloy AlCoCrFeNi2.1, Intermetallics 154 (2023), https://doi.org/10.1016/j.intermet.2023.107822.
[44] S. Li, X. Hou, X. Liu, Z. Liu, X. Wang, T. Wu, Y. Bai, W. Zhao, Microstructure and mechanical properties of electron beam welding of AlCoCrFeNi2.1 eutectic high entropy alloy, Intermetallics 175 (2024), https://doi.org/10.1016/j.intermet.2024.108530.
[45] J. Li, W. Wei, H. Zhang, Z. Yao, M. Chen, X. Zhao, G. Yin, X. Yang, On the investigation of microstructure and mechanical properties of the AlCoCrFeNi2.1/316 L dissimilar spot-welded joint, Mater. Today Commun. 41 (2024), https://doi.org/10.1016/j.mtcomm.2024.110990.
[46] J. Rončák, P. Jozefovič, M. Zobač, Weld Evaluation of Eutectic High-Entropy Alloy and Austenitic Steel Formed by EBW, 2024, pp. 387–393, https://doi.org/10.37904/metal.2024.4905.
[47] M. Ma, W. Wei, H. Zhang, Z. Yao, Y. Sun, M. Chen, F. Wu, Dissimilar gas tungsten arc welding of AlCoCrFeNi2.1 eutectic high entropy alloy to 316L stainless steel, J. Mater. Res. Technol. 35 (2025) 7065–7073, https://doi.org/10.1016/j.jmrt.2025.03.044.
[48] J.-O. Andersson, Thomas Helander, Lars Höglund, Pingfang Shi, Bo Sundman, Thermo-calc and DICTRA, Comput. Tools Mater. Sci. (2002) 273–312.
[49] A.P. Hammersley, FIT2D: a multi-purpose data reduction, analysis and visualization program, J. Appl. Crystallogr. 49 (2016) 646–652, https://doi.org/10.1107/S1600576716000455.
[50] MDI JADE/V 8.7, Materials Data: Livermore, CA, 2022.
[51] S.N. Kabekkodu, A. Dosen, T.N. Blanton, PDF-5+: a comprehensive powder diffraction fileTM for materials characterization, Powder Diffract. (2024), https://doi.org/10.1017/S0885715624000150.
[52] W. Tillmann, A. Eilers, T. Henning, Vacuum brazing and heat treatment of NiTi shape memory alloys, IOP Conf. Ser.: Mater. Sci. Eng. 1147 (2021) 012025, https://doi.org/10.1088/1757-899x/1147/1/012025.
[53] H. Jiang, L. Li, Z. Ni, D. Qiao, Q. Zhang, H. Sui, Effect of Nb on microstructure and properties of AlCoCrFeNi2.1 high entropy alloy, Mater. Chem. Phys. 290 (2022), https://doi.org/10.1016/j.matchemphys.2022.126631.
[54] J.M. Zhu, J.L. Meng, J.L. Liang, Microstructure and mechanical properties of multi-principal component AlCoCrFeNiCux alloy, Rare Metals 35 (2016) 385–389, https://doi.org/10.1007/s12598-014-0268-5.
[55] H. Okamoto, Cu-Nb (copper-niobium), J. Phase Equilib. Diffus. 33 (2012) 344, https://doi.org/10.1007/s11669-012-0051-y.
[56] M.H. Gert den Ouden, Processes, in: G. den Ouden, M.J.M. Hermans (Eds.), Welding Technology, First, VSSD, CA Delft, The Netherlands, 2009, pp. 1–50.

[57] Sindo Kou, Fluid flow and metal evaporation in welding, in: Welding Metallurgy, Second edition, John Wiley & Sons, Inc, Hoboken, New Jersey., 2003, pp. 97–120.
[58] N. Chakraborty, S. Chakraborty, Modelling of turbulent molten pool convection in laser welding of a copper-nickel dissimilar couple, Int. J. Heat Mass Transf. 50 (2007) 1805–1822, https://doi.org/10.1016/j.ijheatmasstransfer.2006.10.030.
[59] C. Tan, K. Zhou, W. Ma, L. Min, Interfacial characteristic and mechanical performance of maraging steel-copper functional bimetal produced by selective laser melting based hybrid manufacture, Mater. Des. 155 (2018) 77–85, https://doi.org/10.1016/j.matdes.2018.05.064.
[60] D.J. Sharar, B.F. Donovan, R.J. Warzoha, A.A. Wilson, A.C. Leff, B.M. Hanrahan, Solid-state thermal energy storage using reversible martensitic transformations, Appl. Phys. Lett. 114 (2019), https://doi.org/10.1063/1.5087135.
[61] T. Wang, F. Cao, P. Zhou, H. Kang, Z. Chen, Y. Fu, T. Xiao, W. Huang, Q. Yuan, Study on diffusion behavior and microstructural evolution of Al/cu bimetal interface by synchrotron X-ray radiography, J. Alloys Compd. 616 (2014) 581–593, https://doi.org/10.1016/j.jallcom.2014.07.172.
[62] M. Way, J. Willingham, R. Goodall, Brazing filler metals, Int. Mater. Rev. 65 (2020) 257–285, https://doi.org/10.1080/09506608.2019.1613311.
[63] X. Chen, W. Xie, J. Zhu, Z. Wang, Y. Wang, Y. Ma, M. Yang, W. Jiang, H. Yu, Y. Wu, X. Hui, Influences of Ti additions on the microstructure and tensile properties of AlCoCrFeNi2.1 eutectic high entropy alloy, Intermetallics (Barking) 128 (2021), https://doi.org/10.1016/j.intermet.2020.107024.
[64] R. Li, W. Sun, S. Li, Z. Cheng, The effect of zirconium on the microstructure and properties of cast AlCoCrFeNi2.1 eutectic high-entropy alloy, Materials 17 (2024) 5938, https://doi.org/10.3390/ma17235938.
[65] W. Sun, R. Zhang, X. Kong, J. Kou, Y. Fu, M. Gao, Interface and mechanical property of cu/AlCoCrFeNi2.1 layered composites prepared by solid/liquid bonding, Mater. Lett. 313 (2022), https://doi.org/10.1016/j.matlet.2022.131792.
[66] S. Katayama, Solidification phenomena of weld metals (1st report). Characteristic solidification morphologies, microstructures and solidification theory, Weld. Int. 14 (2000) 939–951, https://doi.org/10.1080/09507110009549297.
[67] H. Zheng, R. Chen, G. Qin, X. Li, Y. Su, H. Ding, J. Guo, H. Fu, Phase separation of AlCoCrFeNi2.1 eutectic high-entropy alloy during directional solidification and their effect on tensile properties, Intermetallics 113 (2019), https://doi.org/10.1016/j.intermet.2019.106569.
[68] N. Balasubramani, J. Venezuela, D. StJohn, G. Wang, M. Dargusch, A review of the origin of equiaxed grains during solidification under mechanical stirring, vibration, electromagnetic, electric-current, and ultrasonic treatments, J. Mater. Sci. Technol. 144 (2023) 243–265, https://doi.org/10.1016/j.jmst.2022.09.06.
[69] Sindo Kou, Basic solidification concepts, in: Welding Metallurgy, SECOND, John Wiley & Sons, Inc, New Jersey, 2003, pp. 145–169.
[70] W.L. Wang, Z.H. Kong, Phase separation and microhardness of rapidly solidified high-entropy CoCrFeNiCux alloys, J. Alloys Compd. 853 (2021), https://doi.org/10.1016/j.jallcom.2020.156451.
[71] N. Yurchenko, N. Stepanov, G. Salishchev, Laves-phase formation criterion for high-entropy alloys, Mater. Sci. Technol. 33 (2017) 17–22, https://doi.org/10.1080/02670836.2016.1153277.
[72] S. Guo, C.T. Liu, Phase stability in high entropy alloys: formation of solid-solution phase or amorphous phase, Prog. Nat. Sci. Mater. Int. 21 (2011) 433–446, https://doi.org/10.1016/S1002-0071(12)60080-X.
[73] S. Guo, C. Ng, J. Lu, C.T. Liu, Effect of valence electron concentration on stability of fcc or bcc phase in high entropy alloys, J. Appl. Phys. (2011), https://doi.org/10.1063/1.3587228.
[74] K.W. Li, X.B. Wang, W.X. Wang, S.M. Li, D.Q. Gong, H.Z. Fu, Microstructural evolution and compressive properties of two-phase Nb-Fe alloys containing the C14 laves phase NbFe2 intermetallic compound, High Temp. Mater. Processes 35 (2016) 129–134, https://doi.org/10.1515/htmp-2014-0174.
[75] A. Takeuchi, A. Inoue, Classification of bulk metallic glasses by atomic size difference, heat of mixing and period of constituent elements and its application to characterization of the main alloying element, Mater. Trans. (2005), https://doi.org/10.2320/matertrans.46.2817.
[76] S. Guo, C.T. Liu, Phase Stability in High Entropy Alloys: Formation of Solid-Solution Phase or Amorphous Phase, 2026.
[77] J.B. Mann, T.L. Meek, E.T. Knight, J.F. Capitani, L.C. Allen, Configuration energies of the d-block elements, J. Am. Chem. Soc. 122 (2000) 5132–5137, https://doi.org/10.1021/ja9928677.
[78] M.H. Tsai, K.C. Chang, J.H. Li, R.C. Tsai, A.H. Cheng, A second criterion for sigma phase formation in high-entropy alloys, Mater. Res. Lett. 4 (2016) 90–95, https://doi.org/10.1080/21663831.2015.1121168.
[79] E. Bosi, A. Meghwal, S. Singh, P. Munroe, C.C. Berndt, A.S.M. Ang, Empirical and computational-based phase predictions of thermal sprayed high-entropy alloys, J. Therm. Spray Technol. 32 (2023) 1840–1855, https://doi.org/10.1007/s11666-023-01586-2.
[80] T.W.J. de Geus, R.H.J. Peerlings, M.G.D. Geers, Competing damage mechanisms in a two-phase microstructure: how microstructure and loading conditions determine the onset of fracture, Int. J. Solids Struct. 97_98 (2016) 687–698, https://doi.org/10.1016/j.ijsolstr.2016.03.029.